PHYSICAL REVIEW B **105**, 035408 (2022)

Stability and electronic properties of monolayer and multilayer structures of group-IV elements and compounds of complementary groups in biphenylene network

Salih Demirci,[1] Şafak Çallıoğlu,[2,3] Taylan Görkan,[4] Ethem Aktürk,[4,5,*] and Salim Ciraci[3,†]
[1]*Department of Physics, Kırıkkale University, Kırıkkale 71450, Turkey*
[2]*Department of Electrical and Electronic Engineering, Bilkent University, Ankara 06800, Turkey*
[3]*Department of Physics, Bilkent University, Ankara 06800, Turkey*
[4]*Department of Physics, Adnan Menderes University, 09100 Aydin, Turkey*
[5]*Physik Department E20, Technische Universität München, 85748 Garching, Germany*

(Received 13 July 2021; revised 22 November 2021; accepted 22 December 2021; published 7 January 2022)

We predict that specific group-IV elements and IV-IV, III-V, and II-VI compounds can form stable, freestanding two-dimensional (2D) monolayers consisting of octagon, hexagon, and square rings (ohs), in which the threefold coordination of atoms is preserved to allow sp^2-type hybridization. These monolayers can also construct bilayers, multilayers, three-dimensional (3D) layered van der Waals solids, and 3D crystals with strong vertical bonds between layers as well as quasi-one-dimensional nanotubes and nanoribbons with diverse edge geometries. All these ohs structures can constitute a large class of 2D materials ranging from good metals to wide bandgap semiconductors and display physical and chemical properties rather different from those of their counterparts in the hexagonal (honeycomb) network. The metallic state of freestanding 2D C, Si, and Ge ohs monolayers and 3D C ohs bulk contrast, respectively, with graphene, silicene, germanene, and graphite.

DOI: 10.1103/PhysRevB.105.035408

I. INTRODUCTION

Following the synthesis of graphene [1], a planar, freestanding two-dimensional (2D) monolayer of carbon in a honeycomb network of perfectly sp^2-hybridized atoms, several nanomaterials constituted from group-IV elements and IV-IV and III-V compounds have been predicted theoretically [2], and most of them have been synthesized. Unveiling physical and chemical properties of those 2D structures and their possible three-dimensional (3D) layered van der Waals (vdW) solids has dominated research in nanoscience for the last two decades. Recently, Fan *et al.* [3] synthesized quasi-one-dimensional (1D) nanoribbons of carbon in the biphenylene network on an Au(111) surface, which consist of the adjacent octagon, hexagon, and square rings, specified briefly as *ohs structure*. This is a very important achievement realizing a metallic, nonhexagonal, nanosized monolayer of carbon that had been proposed/predicted in various theoretical studies [4–7].

In this paper, we study 2D monolayers of group-IV elements and IV-IV, III-V, and II-VI compounds in the periodic ohs structure by calculating their optimized atomic structures and mechanical and electronic properties and performing extensive dynamical and thermal stability analyses using density functional theory (DFT). We predicted that, like C [4], Si, and Ge, their compounds SiC, GeC, and SnC and III-V compounds like BN [8], BP, BAs, BSb, AlN, GaN, and InN can form stable/robust, freestanding (unsupported) 2D ohs monolayers with physical and chemical properties differing from their allotropes in the honeycomb (hexagonal) network. While most of the III-V compounds in the ohs network are planar, specific III-V and II-VI compounds like BAs, BSb, AlP, and ZnSe display unusual structural features; they are buckled (puckered) in wavy forms. While 2D Si and Ge ohs monolayers are metals, the compounds are semiconductors with direct bandgaps. In these 2D ohs monolayers, atoms are threefold coordinated like their counterparts in the hexagonal network, but the associated sp^2 hybridizations of atomic orbitals are deformed, which underlie differences in mechanical and electronic properties between two different networks. The 2D ohs monolayers can also form quasi-1D nanotubes and nanoribbons with diverse edge geometries. More importantly, when stacked, some of these 2D ohs monolayers can form stable bilayers, multilayers, and stable 3D layered structures like graphite with weak interlayer binding interaction consisting of mainly vdW attraction. Interestingly, a weak, vertical chemical interaction sets in between the layers of C ohs bilayer and multilayers. Conversely, in specific bilayers and multilayers like Si, Ge ohs, and compounds like GaN ohs, strong vertical bonds are constructed between layers, forming a network of connected octagon and square rings in the side view. Here, 3D layered C ohs, which is the analog of graphite and apparently a 3D allotrope of carbon in addition to well-known diamond and graphite, is highly metallic with significant state density at the Fermi level. In this paper, we present our results, which unveil a large class of materials together with their unusual properties.

II. METHOD

DFT calculations were carried out using VASP [9] packages. Projector-augmented wave potentials [10] and the

---

[*] ethem.aktuerk@tum.de
[†] ciraci@fen.bilkent.edu.tr

exchange-correlation potential within the generalized gradient approximation with the Perdew, Burke, and Ernzerhof (PBE) functional [11] have been used. Wave functions are expanded in plane-wave basis sets up to the electron kinetic energy cutoff of 520 eV. Brillouin zone (BZ) integration was performed with an automatically generated $12 \times 14 \times 1$ k-point grid in the Monkhorst-Pack scheme [12]. Ionic relaxation was realized by a conjugate gradient algorithm, which optimizes structure. All atoms in the supercell were fully relaxed until the energy difference between the successive steps was $<10^{-5}$ eV and the force on each atom was $<10^{-2}$ eV/Å. In addition, maximum pressure on the lattice was lowered down to 0.1 kbar. We also applied the Heyd-Scuseria-Ernzerhof (HSE06) hybrid functional method [13] to obtain corrected band values. The HSE06 functional is constructed by mixing 25% of the Fock exchange with 75% of the PBE exchange and 100% of the PBE correlation. vdW corrections were included using the Becke-Jonson (BJ) damping in the DFT-D3 method [14,15].

The dynamical stability analysis was performed by using two different methods, namely, small displacement and density functional perturbation theory, to calculate phonon spectra with and without vdW correction, respectively [16,17]. Phonon calculations were carried out on $4 \times 5 \times 1$, $2 \times 3 \times 1$, and $3 \times 4 \times 4$ supercells for optimized monolayer, bilayer (multilayer), and 3D layered structures, respectively. These structures, having vibration modes with frequencies $\omega^2 > 0$ for all k in the first BZ, were considered to be stable. The thermal stability of these systems was tested by *ab initio* molecular dynamics (AIMD) calculations at finite temperature. The time step between ionic iterations was taken to be 2 fs. After every 50 steps, velocities were rescaled to match the desired temperature. Charge density isosurfaces of selected band states and some mechanical properties were obtained using VASPKIT [18]. Atom projected density of states, shown as the inset in Fig. 1(g), was plotted by PYPROCAR [19].

The cohesive energy (per atom) of any ohs monolayer including n atoms in the cell was calculated as $E_c(\text{ohs}) = [nE_T(\text{atom}) - E_T(\text{ohs})]/n$. The binding interaction energy (per atom) of any ohs multilayer with N layers is $E_{ib}(N-\text{ohs}) = N * E_c(\text{ohs}) - E_c(N-\text{ohs})$ where, for the sake of consistency, both E_c values (multilayer and monolayer) were calculated with vdW correction. Mechanical properties were calculated by applying strain between -1 and $+1\%$ in steps of 0.25%, and atomic positions were relaxed at each strained step. The elastic strain energy per unit area is expressed using Voight notation [20] and can be expressed by the following expression: $U(\epsilon_x, \epsilon_y) = \frac{1}{2}C_{11}\epsilon_x^2 + \frac{1}{2}C_{22}\epsilon_y^2 + C_{12}\epsilon_x\epsilon_y$, where $\epsilon_x(\epsilon_y)$ is strain in the $x(y)$ direction, and C_{11}, C_{22}, and C_{12} are elastic constants. Due to anisotropy, $C_{11} \neq C_{22}$. For 2D materials, the mechanical properties are expressed by in-plane Young's modulus (or stiffness) (Y) and Poisson's ratio (ν), which can be written in the x (y) direction as $Y_x = (C_{11}C_{22} - C_{12}C_{21})/C_{22}$ [$Y_y = (C_{11}C_{22} - C_{12}C_{21})/C_{11}$] and $\nu_x = C_{12}/C_{22}$ ($\nu_y = C_{12}/C_{11}$). We first calculated in-plane Young's modulus of graphene (in which case $Y_x = Y_y$) and found it to be 341.89 J/m^2, which is in a good agreement with the value in the literature 340 J/m^2 [21].

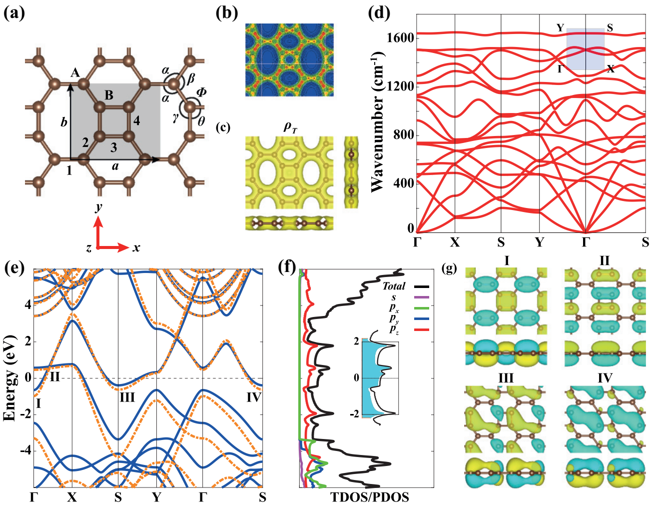

FIG. 1. (a) Optimized atomic structure of a two-dimensional (2D) C octagon-hexagon-square (ohs) monolayer with two types of carbon atoms A and B. The rectangular primitive unit cell with lattice constants **a** and **b** is delineated. Different bonds are indicated by numerals, and bond angles α, β, γ, ϕ, and θ deviating from $2\pi/3$ are shown. (b) Total charge density $\rho_T(\mathbf{r})$ contour plots in a lateral plane passing through different types of bonds. (c) Isosurfaces of $\rho_T(\mathbf{r})$ with side views. (d) Phonon dispersion curves along different directions of the rectangular Brillouin zone (BZ) demonstrate the dynamical stability. (e) Electronic energy band structure calculated within PBE. Bands calculated by HSE are shown by dashed lines. Zero of the energy is set to E_F shown by a dotted line. (f) The corresponding total (TDOS) and s- and $p_{x,y,z}$-orbital projected density of states (PDOS). The inset shows the projection of TDOS near E_F to four carbon atoms situated at the corners of the square ring. (g) Isosurfaces of selected band states $\Psi_{n,k}(\mathbf{r})$ indicated in (e). Positive (negative) values are shown in yellow (turquoise) color.

III. RESULTS AND DISCUSSIONS

In this section, we study the optimized atomic structures, test their stability and binding, and discuss their electronic properties.

A. 2D monolayers

In Fig. 1(a), the optimized 2D C ohs structure in planar geometry together with the analysis of its charge density is shown. This can also be taken as a prototype top view of any 2D ohs monolayer with different structural parameters. While the planar geometry is also maintained for some compounds involving at least one element from the first row of the periodic table, it is destroyed for others like 2D Si, Ge ohs due to weakening of π bonds with increasing bond length. At the end, these two structures underwent a complex buckling, where their atoms are located in four different lateral planes leading to three different buckling distances Δ_i, $i = 1$–3, as shown in Fig. 2(a). Although all atoms of the ohs structures are threefold coordinated, the bond angles deviate from $2\pi/3$ depending on their neighborhood with different rings, buckling, and ionicity. Accordingly, one distinguishes two different types of atoms in 2D C, Si, and Ge ohs monolayers,

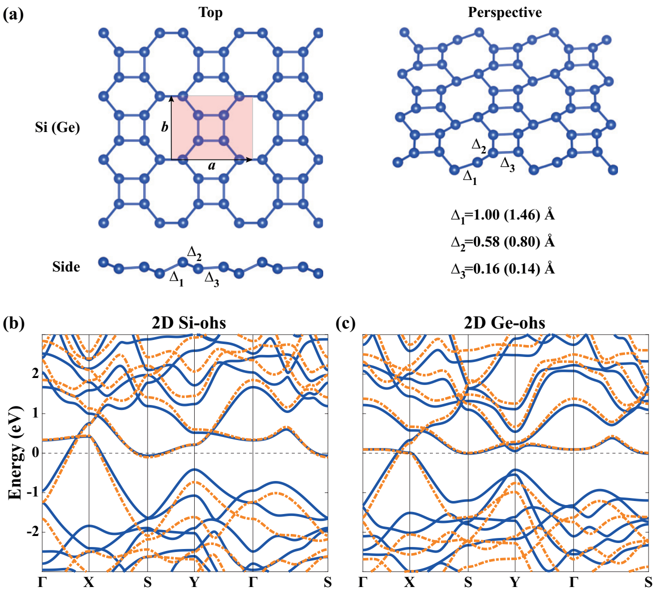

FIG. 2. (a) Top, side, and perspective views of the optimized atomic structure of a two-dimensional (2D) Si(Ge) octagon-hexagon-square (ohs) monolayer. Three different buckling parameters Δ_i, $i = 1$–3, are indicated in the side and perspective view. (b) Electronic energy band structure of a 2D Si ohs monolayer calculated within PBE and HSE (dashed lines) indicates a metallic state. (b) Same for 2D Ge ohs. Zero of the energy is set to E_F shown by a dotted line.

each forming deformed sp^2-hybridized bonds: one, denoted by A, is at the corner of two *o* and one *h* rings; the second one B is at the corner of adjacent *o*, *h*, and *s* rings with different bond angles. For 2D compound ohs structures, the situation is complex since A- and B-type atoms correspond to different elements with different ionicity and effective charge. Bonds (their lengths ranging from 1.41 to 1.47 Å) and bond angles (ranging from 90° to 145°) of 2D C ohs in planar geometry are indicated in Fig. 1(a). The contour plots of charge density $\rho_T(\mathbf{r})$ in Fig. 1(b) reflect the deviations from the perfect sp^2 hybridization and from the regular π bonding. These A- and B-type atoms are also distinguished by their different chemical activities and point defect formation. For example, the chemisorption energy of a hydrogen atom to B-type carbon is 0.9 eV higher, but the resulting magnetic moment is 0.3 μ_B smaller. Apparently, owing to A- and B-type carbon atoms, a 2D C ohs monolayer acquires a site-specific chemical activity and the ability of coverage for functionalization to attain unique chemical, mechanical, optoelectronic, and magnetic properties. Owing to their bucklings, 2D Si and Ge ohs monolayers can display even more complex behavior. Nevertheless, on a 2D Si ohs monolayer, an H atom attains 0.4 eV stronger binding at the B-type atom than that at the A-type atom. In Table I, the optimized values of relevant structural parameters, cohesive energy E_c, and the state of stable 2D ohs monolayers are presented. Here, we placed emphasis on the 2D C ohs monolayer since it was synthesized recently being an allotrope of carbon as a counterpart of graphene. In Table II, we present the calculated values of relevant structural parameters, cohesive energy, and mechanical properties of 2D C ohs monolayer, bilayer, and 3D bulk and compare them with other well-known allotropes of a carbon atom.

The dynamical stability of all freestanding 2D ohs monolayers treated in this paper is proven by the calculated vibration frequencies, with $\omega^2 \geqslant 0$. Additionally, their thermal stabilities above room temperature are assured through AIMD calculations carried out at temperatures as high as $T = 900$ K. Accordingly, the freestanding 2D ohs monolayers reported in this paper keep their stability at high temperatures. Further to these stability analyses, the cohesive energy per atom (E_c) of the 2D ohs monolayers are calculated to be positive, favoring the ohs structure relative to free constituent atoms. For example, a 2D C ohs with $E_c = 7.50$ eV/atom has a Born-Oppenheimer surface with its minimum placed 0.46 eV above that of graphene. This is in agreement with a previous study on a 2D C ohs monolayer [6]. Calculated values of elastic properties of these 2D monolayers also support that they are freestanding and robust structures to be considered as 2D allotropes of parent elements. As an example, the in-plane stiffnesses of 2D C ohs $Y_x = 202.55$ J/m^2 and $Y_y = 236.68$ J/m^2 are rather high, even if they are lower than those of a graphene monolayer (see Table II). Conversely, the values of Poisson's ratio are higher than

TABLE I. Calculated values for 2D ohs monolayers of group-IV elements and IV-IV and III-V planar compounds. Columns: Material (element or compound); lattice constants in angstroms; buckling in angstroms; cohesive energy E_c in electronvolts per atom; state of the monolayer: M = metal, S = semiconductor with the energy band gap E_g in electronvolts.

Material	Lattice constants **a**, **b** (Å)	Buckling Δ_1, Δ_2, Δ_3 (Å)	E_c (eV/atom)	State
2D C ohs	4.52, 3.76	0	7.50	M
2D Si ohs	7.15, 5.72	1.00, 0.58, 0.16	3.82	M
2D Ge ohs	7.51, 6.03	1.46, 0.80, 0.14	3.13	M
2D SiC ohs	5.61, 9.44	0	5.76	S/2.15 eV
2D GeC ohs	5.96, 9.96	0	4.68	S/1.72 eV
2D SnC ohs	6.57, 11.01	0	4.04	S/1.08 eV
2D BN ohs	4.55, 7.66	0	6.81	S/4.49 eV
2D BP ohs	5.90, 9.76	0	4.75	S/0.24 eV
2D AlN ohs	5.62, 9.60	0	5.09	S/3.53 eV
2D GaN ohs	5.90, 9.96	0	3.83	S/2.65 eV
2D InN ohs	6.59, 11.12	0	3.05	S/1.13 eV

TABLE II. Calculated values of 2D C ohs monolayer, bilayer, and 3D layered C ohs (bulk). Corresponding values for 2D graphene monolayer, its bilayer, and 3D graphite are also included for the sake of comparison. Columns: Lattice constants in angstroms; cohesive energy E_c (calculated with vdW/without vdW) in electronvolts per atom; Young's modulus Y_x and Y_y in Joules per square meter for 2D, in gigaPascals for 3D. The same units are also for bulk modulus K for 2D and 3D structures, respectively; Poisson's ratio ν_x and ν_y (%); bulk modulus K; electronic state (M = metal, SM = semimetal). Experimental or calculated values taken from previous publications are shown in parentheses with pertaining references.

	Lattice constant (Å)	E_c	Y_x	Y_y	ν_c	ν_y	K	State
2D C ohs monolayer	$a = 4.52$ $b = 3.76$	7.57/7.50	202.55	238.68	0.35	0.41	185.81	M
2D C ohs bilayer	$a = 4.52$ $b = 3.77$	7.59	425.97	484.68	0.32	0.37	366.92	M
3D C ohs	$a = 4.52$ $b = 3.77$ $c = 3.35$	7.62	609.52	713.75	0.34	0.40	31.17	M
2D graphene	$a = 2.47$ $b = 2.47$	8.05/7.96	341.89 (340)[a] (342.2)[c]	341.89 (340)[a] (342.2)[c]	0.17 (0.17)[b] (0.17)[c]	0.17 (0.17)[b] (0.17)[c]	209.47 (216.0)[c] (206.1)[d]	SM
2D graphene bilayer	$a = 2.47$ $b = 2.47$	8.08	700.54 (703.1)[c]	700.54 (703.1)[c]	0.19 (0.186)[c]	0.19 (0.186)[c]	439.07 (432.2)[c]	SM
3D graphite	$a = 2.47$ $b = 2.47$ $c = 6.76$	8.10	1042.77 (1023)[e]	1042.77 (1023)[e]	0.20 (0.16)[e]	0.20 (0.16)[e]	31.47 (30.1)[f] (33.8)[g]	SM

[a] Reference [21].
[b] Reference [22].
[c] Reference [20].
[d] Reference [23].
[e] Reference [24].
[f] Reference [25].
[g] Reference [26].

graphene, but they display some directionality. Here, we point out another important structural feature that the resistance of a 2D C ohs monolayer against the penetration/transmission of an oxygen atom or molecule is calculated to be rather high (∼24 eV). This suggests that this monolayer can be used as an antioxidant coating to prevent solid surfaces from corrosion.

The energy bands of graphene, silicene, and germanene of a honeycomb network, which are crossed linearly at the Fermi level E_F, underwent significant changes in the 2D ohs structure, as shown in Figs. 1(e), 2(b), and 2(c). Multiple crossings of the Fermi level by the bands lead to significant state density at the Fermi level $D(E = E_F)$, which attributes metallicity to these monolayers, as shown in Fig. 1(d) for the C ohs monolayer. The metallic state, which originates mainly from the bands derived from carbon p_z orbitals located at the corners of the square rings is further confirmed by the inset in Fig. 1(f). The character of the wave function $\Psi_{n,k}(\mathbf{r})$ of the selected states in Fig. 1(g) corroborate the projected DOS (PDOS) and reveals the orbital character of the states near the Fermi level. Bonding and antibonding combination of p_z orbitals of neighboring atoms are clearly seen. The calculated work function of a 2D C ohs monolayer $\Phi = 4.26$ eV is 0.30 eV smaller than that of graphene [27].

The III-V compounds SiC, GeC, SnC, BP, BN, AlN, GaN, and InN in planar ohs monolayer structures are direct bandgap semiconductors with bandgaps ranging from 0.24 to 4.49 eV according to HSE calculations. In Fig. 3, we present the energy band structure of these 2D ohs monolayers of compounds around the Fermi level. Like h-BN, a BN ohs monolayer has a wide bandgap; thin sheets of it can serve as an insulator. The direct bandgaps of these nanostructures gain importance in various optoelectronic applications. Here, GaN and InN ohs monolayers appear to be convenient to produce nanoelectronic devices. However, specific III-V and II-VI compounds in an ohs network like BAs, BSb, AlP, and ZnSe display unusual and peculiar structural features; their buckled structures by themselves show periodic, wavy forms. This is due to increased difference between their p_z orbitals of anions and cations leading to this intermediate minimum energy configuration maintaining stability.

B. Zero-dimensional and quasi-1D structures

These 2D ohs monolayers, particularly the 2D C ohs monolayer, can form zero-dimensional (0D) flakes and also quasi-1D nanoribons [5] with or without parent edge atoms being saturated. Normally, these are finite-sized structures of 2D periodic monolayers in lower dimensionality. In fact, the structure synthesized by Fan *et al.* [3] was not a large C ohs monolayer; it was rather a nanoribbon. In the past, nanoribbons of various 2D monolayers having the hexagonal network (like graphene, silicene, and h-BN) have been extensively

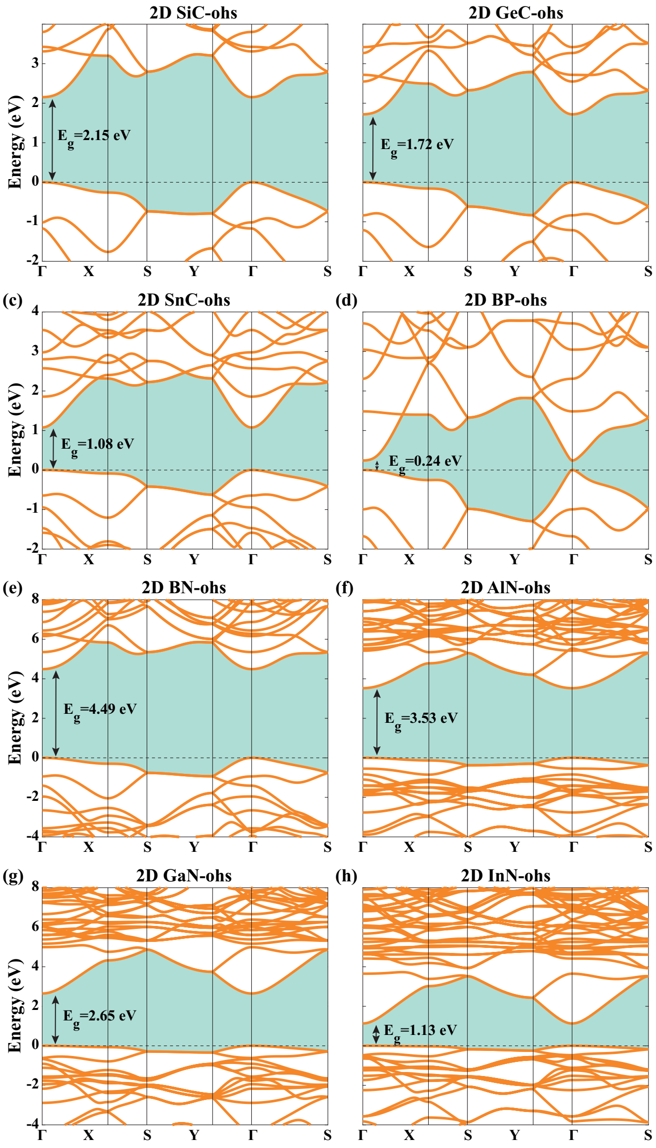

FIG. 3. Electronic energy band structures of planar two-dimensional (2D) monolayers of IV-IV and III-V compounds calculated within HSE are shown around the energy bandgap. The bandgap is shaded, and zero of energy is set to the top of the valence band.

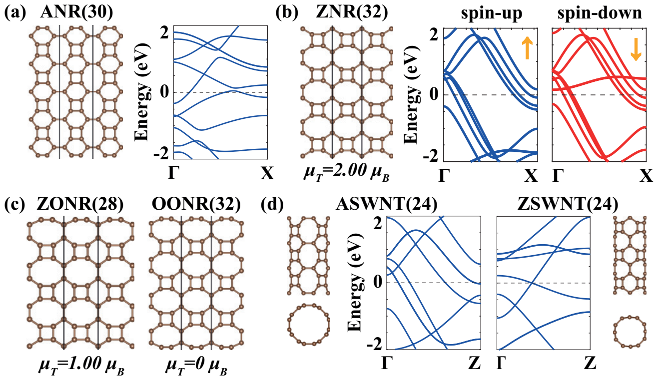

FIG. 4. (a) An armchair nanoribbon (ANR) comprising 30 carbon atoms in the unit cell. The calculated energy band structure on the one-dimensional (1D) Brillouin zone (BZ) along k_x parallel to its axis indicates a metallic state. (b) Zigzag nanoribbon (ZNR) having magnetic moment of $\mu_T = 2.0\ \mu_B$/cell, and its spin-polarized energy bands indicate magnetic metallic state. (c) Two nanoribbons with zigzag-octagon (ZONR) and octagon-octagon edges (OONR). The former nanoribbon has a magnetic moment of $\mu_T = 1.0\ \mu_B$/cell. (d) Atomic structure of single-walled armchair (ASWNT) and zigzag (ZSWNT) nanotubes of C octagon-hexagon-square (ohs) with their metallic band structures.

treated since they display electronic and magnetic properties different from parent periodic monolayers depending on their edge geometries, widths, and foreign atoms saturating their edges. As predicted earlier [6] and confirmed experimentally [3], the C ohs nanoribbons may undergo metal-insulator transition as their widths decrease. Notably, based on differential conductance dI/dV spectra, Fan *et al.* [3] found that the bandgap of narrow nanoribbons of C ohs is closed, as their width increase, and hence, wide nanoribbons turn to be metallic. The nanotubes and nanoribbons of ohs structure are beyond the scope of this paper. Here, we only point out an important feature related with nanoribbons of C ohs. We found that nanoribbons of C ohs are superior to the nanoribbons of graphene since the former provide more alternatives in their edge geometries, like both sides being zigzag, armchair, octagonal or octagonal-zigzag, octagonal-square, etc. As shown in Figs. 4(a) and 4(b), freestanding armchair (with both edges constructed from hexagon rings) and zigzag (both edges constructed from square and hexagon rings) nanoribbons of C ohs, as an example, are both metallic, but the latter is magnetic with a magnetic moment of $\mu = 2.0\ \mu_B$ per cell. Incidentally, one can monitor the magnetization of nanoribbons of an ohs structure depending on whether its edges consist of double octagons or a single octagon. In Fig. 4(c), while the C ohs nanoribbon with octagon and zigzag edges is magnetic with $\mu = 1.0\ \mu_B$ per cell, one with both octagon edges is nonmagnetic. The edge states of zigzag and octagonal-square nanoribbons are analyzed in the forthcoming section. In this paper, we have proven that ohs monolayers can also form stable, single-walled nanotubes. For example, as described in Fig. 4(d), by wrapping a C ohs nanoribbon around a cylinderso that its zigzag (armchair) edges parallel the axis of the cylinder, one produces a zigzag (armchair) single-wall nanotube of C ohs structure [6].

C. Bilayer and multilayers

By stacking 2D ohs monolayers, one can construct bilayers and multilayers. The bilayer of 2D C ohs is of particular interest. Among various registries of stacking, the on-top registry (A-A stacking) has the lowest energy, even though the difference of binding energies between various registries is minute. In Fig. 5(a), the bilayer constructed from two 2D C ohs monolayers is described. In this paper, we reveal that, upon the formation of the bilayer, the electronic charge from the center of the square ring is oozed to the middle of two monolayers by opening a hole at the center of the square rings [compare Fig. 1(c) with Fig. 5(b)]. This way a weak, vertical chemical bond is constructed in addition to the attractive vdW interaction. This situation is better described

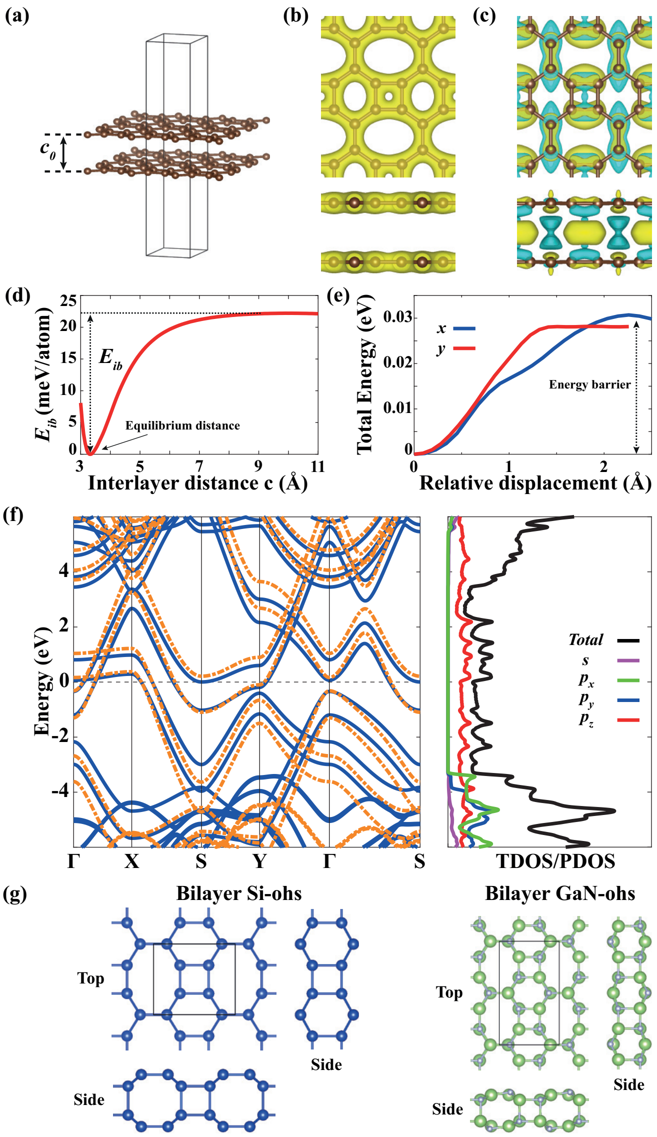

FIG. 5. (a) Atomic structure of the C octagon-hexagon-square (ohs) bilayer with the equilibrium interlayer distance of $c_o = 3.31$ Å, which is close to that of graphene. (b) The top and side views of the isosurfaces of the total charge density $\rho_T(\mathbf{r})$. (c) The same for the difference charge density $\Delta\rho(\mathbf{r})$, indicating charge transfer to the region between the squares of both layers. Regions of charge accumulation (depletion) are shown by yellow (turquoise) color. (d) The relative binding energy with respect to interlayer distance. (e) Variation of the total energy with relative lateral displacements of two layers along x and y axes. (f) Energy band structure and corresponding total (TDOS) and projected (PDOS) densities of states of the bilayer. HSE bands are indicated by dashed lines, and the zero of energy is set to E_F. p_z orbitals have pronounced contribution to the state density at the Fermi level $D(E_F)$. (g) Bilayer structures of Si, and GaN ohs. Side views consist of connected octagon and square rings made by strong lateral and vertical bonds.

by the difference charge density $\Delta\rho(\mathbf{r})$, where the monolayer charge densities are subtracted from the total charge density. Because of this weak and vertical bond, the top and bottom square rings in different layers are slightly pulled together, causing a local buckling and hence slight narrowing of the interlayer distance by 0.03 Å. The severe deformation of sp^2 hybridization by reducing the bond angle from $2\pi/3$ to $\pi/2$ at the corners of the square ring leads to the formation of a vertical chemical bond. Such a weak chemical bond attributes a special meaning to ohs multilayers. In Fig. 5(d), the variation of the total energy of the bilayer is shown as a function of the interlayer spacing c. The interlayer binding energy is deduced as $E_{ib} = 22$ meV/atom, which appears to be close to that of the graphene bilayer ($\sim$23 meV/atom) with AB stacking (see Table II). The interlayer binding energy of the graphene bilayer calculated using the diffusion quantum Monte Carlo method [28] was predicted to be 17.7 meV/atom.

The variation of the total energy of the C ohs bilayer with the displacement of the top layer relative to the bottom layer along x and y axes is shown Fig. 5(e). The related energy barriers in these lateral displacements are calculated to be only $\sim$30 meV/cell, which are rather low, like the graphene bilayer [29]. This is an important finding, indicating a very low friction constant in the relative sliding motion between two C ohs monolayers.

The electronic structure of the C ohs bilayer is simply a duplicate of constituent 2D monolayers with an energy shift due to the weak interlayer interaction. Accordingly, it is a metal. BN ohs monolayers can form a similar bilayer bound by the attractive vdW interaction. In contrast to the stable bilayers and multilayers of 2D C ohs or BN ohs formed mainly by vdW interaction, the strong vertical chemical interaction between the layers of the Si ohs bilayer causes the interlayer spacings to close and form strong vertical chemical bonds, as shown in Fig. 5(g). For this reason, the electronic structure of the Si ohs bilayer is dramatically different from its monolayer. GaN, AlN ohs bilayers behave similarly. Thus, Si, Ge, and compounds like GaN and AlN ohs monolayers can form neither vdW bilayers nor vdW multilayers made by widely spaced and weakly interacting monolayers. Hence, the atoms of their bilayers and multilayers also form connected octagon and square rings made by strong vertical and lateral bonds, as shown in the side view of Fig. 5(g).

In addition to the C ohs bilayer, we also investigated three-, four-, and five-layer C ohs multilayers. Here, one expects that, as the number of layers increases, the interlayer distance slightly decreases due to increasing vdW interaction. In fact, the interlayer distance of the graphene bilayer of 3.45 Å decreases to 3.38 Å in graphite, in compliance with this argument. However, this trend is reversed in C ohs multilayers: The interlayer distance of the C ohs bilayer increases in multilayers. For example, it increases from 3.31 to 3.35 Å in 3D C ohs. This paradoxical situation is explained by further diminishing of weak vertical chemical bonds between two square rings of the adjacent layers in the on-top position. As for the work function, it increases also with the layer number and saturates at $\Phi = 4.31$ eV.

D. 3D layered ohs structures

Finally, we consider the multilayer formed by the A-A stacking of infinitely many C ohs monolayers to form a layered 3D C ohs structure with translational periodicity perpendicular to the monolayers. This structure is analogous to graphite (formed by the A-B-A ...stacking of graphenes). Its

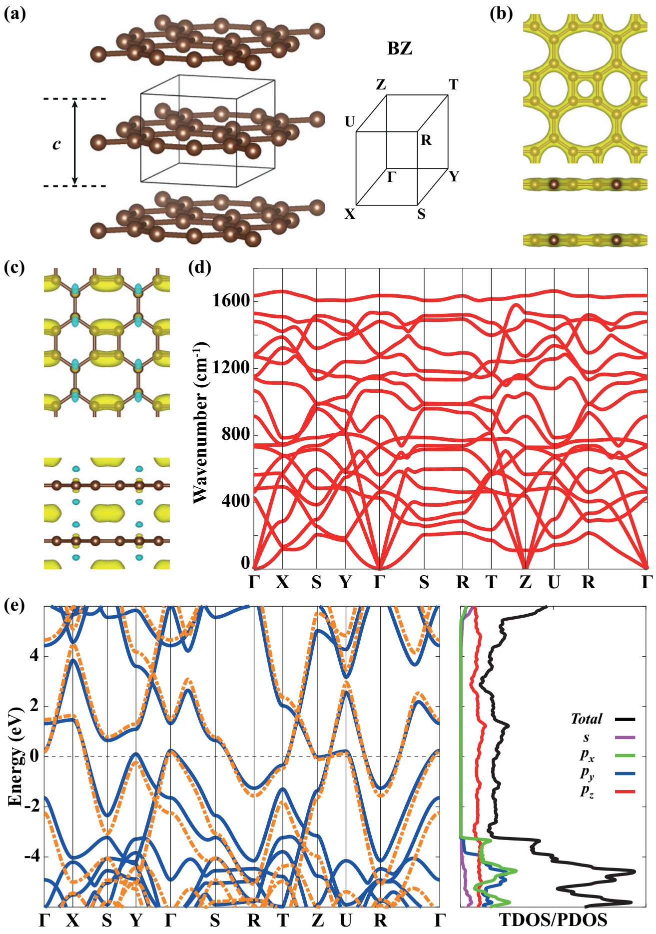

FIG. 6. (a) Optimized atomic structure of the periodic, three-dimensional (3D) C octagon-hexagon-square (ohs) with corresponding primitive unit cell and Brillouin zone (BZ). (b) Top and side views of the isosurfaces of the total charge density $\rho_T(\mathbf{r})$. (c) The same for the difference charge density $\Delta\rho(\mathbf{r})$. (d) Calculated phonon frequencies and their bands along the symmetry directions of the BZ. (e) Calculated electronic energy bands together with total (TDOS) and orbital projected (PDOS) densities of states. Bands calculated by HSE are indicated by dashed lines, and the zero of energy is set to E_F. p_z orbitals have pronounced contribution to the state density at the Fermi level $D(E_F)$.

optimized atomic structure is described in Fig. 6(a). It has the cohesive energy $E_c = 7.62$ eV/atom, which is higher than that of the 2D C ohs monolayer as well as the C ohs bilayer owing to the weak interlayer interaction. The interlayer binding energy is $E_{ib} = 49$ meV/atom. Using the same method, the interlayer binding energy of graphite is calculated to be $E_{ib} = 53$ meV/atom, which is in good agreement with previous studies [30]. The difference charge density in Fig. 6(c) indicates that a weak and vertical chemical bond between square rings continues to contribute to the vdW interlayer binding. This implies also a significant electrical conductivity in the direction perpendicular to the layers. Calculated phonon frequencies in Fig. 6(d) assure that 3D C ohs is dynamically stable. According to the thermal stability analysis using AMID calculations, 3D layered C ohs keeps its stability at high temperatures.

Like its 2D C ohs monolayer, 3D layered C ohs is a robust structure. Its bulk modulus is calculated to be 31.17 GPa, which is slightly smaller than the bulk modulus of graphite 31.47 GPa (the experimental value of 33.8 GPa) [26]. These data indicate that 3D layered C ohs is an allotrope of carbon, like diamond and graphite, even if it does not exist in nature freely. Interestingly, in contrast to insulating diamond and semimetallic graphite, this allotrope is a metal with a significant state density at E_F, as demonstrated in Fig. 6(e).

As for 3D layered BN ohs with AB stacking, it is also a stable, wide bandgap vdW solid. In contrast to these 3D layered C and BN ohs vdW solids, strong vertical chemical bonds between layers prevent the formation of 3D layered Si and Ge ohs vdW solids with weak interlayer interaction. A similar situation also occurred when one started from their 2D monolayers, namely, silicene and germanene in the honeycomb network [31]. Interestingly, the side view of the multilayer metallic Si deformed ohs structure predicted by Görkan *et al.* [32] exhibits close similarity to the top view of the 2D Si ohs monolayer. This similarity may lead to a method for the synthesis of the 2D Si ohs monolayer in future.

IV. DISCUSSIONS AND CONCLUSIONS

Based on numerous properties unveiled in this paper, one can infer the following critical applications of ohs structures: (i) Metallicity of the 2D C ohs monolayer, multilayers, and 3D C ohs is an important property that can be utilized in various technological applications. The C ohs monolayer, being a strictly 2D metal consisting of a single atomic plane, can be considered an ideal system for the quantized conductance showing well-defined quantum steps. In this respect, one expects to observe critical features like quantized conductance in the study of the electronic and heat transport of the 2D C ohs monolayer and the 3D C ohs structure. (ii) IV-IV, III-V, and II-VI compounds and their lateral heterostructures with their bandgaps varying in a wide range of energy can offer critical optoelectronic applications. (iii) Also, alternating stacking of metallic C ohs multilayers and wide bandgap h-BN or BN ohs multilayers to form vertical heterostructures may offer interesting applications. Resonant tunneling double-barrier structures can also be constructed from a junction like C ohs/BN ohs/$n(p)$-type doped InN ohs/BN ohs/C ohs. Vertical heterostructures, like 2D C ohs/BN ohs, Si ohs/SiC ohs can make effective metal/insulator (semiconductor) junctions leading to the formation of the Schottky barrier and hence diode applications. Similar diodes can be realized by the in-plane heterostructures of 2D C ohs/2D BN ohs since they are almost lattice matched. Similar diodes have been proposed earlier through the metal/semiconductor junctions of transition metal dichalcogenides [33]. Similarly, nanocapacitors constructed by the junctions of C ohs/BN ohs/C ohs can realize high-capacity charge and energy storage comparable with that provided by supercapacitors [34]. Not only vertical heterostructures (or junctions) but also periodically repeating, lateral heterostructures of C ohs nanoribbons with those of BN ohs can construct composite materials or junctions. (iv) Not only heterostructures but also adsorption of various adatoms to a 2D ohs structure can lead to the functional surfaces with different magnetic and electronic states and hence deserves further investigations. (v) Apart from electronic applications, one can realize nearly frictionless sliding in the relative motion of two 2D C ohs monolayers since the energy barrier in their relative translational (or sliding) motion is predicted to be rather low. This suggests that surfaces of metals coated by C ohs monolayers can acquire an ability to do relative sliding almost without friction. A similar property of graphene was utilized in the nearly frictionless metal surfaces coated by graphene sheets [29]. (vi) Even if 2D C ohs and BN ohs monolayers appear to be open structures as compared with their counterparts in the hexagonal network, these two structures have high resistance against the penetration of an oxygen atom and molecule through these structures. Accordingly, 2D C, BN ohs monolayers or flakes can be utilized for preventive coating solid surfaces against corrosion.

In conclusion, specific group-IV elements and IV-IV, III-V, and II-VI compounds can form stable, freestanding 2D monolayers consisting of adjacent ohs rings, which preserve the threefold coordination of constituent atoms. These 2D ohs structures make a class of nanomaterials, which are the counterparts of the ones having a honeycomb network, such as graphene, silicene, germanene, h-BN, h-SiC, h-GaN, etc. Depending on the positions of constituent elements in the periodic table, they can be in a planar or buckled geometry; a few of them are buckled over a wavy form around a flat plane. These 2D ohs monolayers display physical and chemical properties different from their counterparts. While 2D ohs monolayers of group IV elements like C, Si, and Ge ohs are metallic with unfilled p_z bands crossing the Fermi level, the compounds, on the other hand, are semiconductors with direct bandgaps ranging from 0.24 to 4.49 eV. They can also make quasi-1D nanotubes and nanoribbons; some of them can undergo metal-insulator transition as their widths change. They construct bilayers, multilayers, 3D layered C ohs and BN ohs structures as vdW solids, and 3D layered crystals with strong vertical bonds between layers. In addition to the pronounced vdW interaction, the formation of vertical, weak chemical bonds between the layers of the C ohs bilayer and multilayers is noteworthy. However, these vertical chemical bonds between the layers of Si, Ge, GaN, and AlN ohs bilayers and multilayers are strengthened and provide a strong interlayer binding. The metallicity of the 2D C ohs monolayer and 3D layered C ohs is an important result because, not only do they constitute metallic allotropes of carbon, but they also may have potential applications in graphene electronics. We believe that our findings in this paper will expand the properties of the classes of 2D nanomaterials.

ACKNOWLEDGMENTS

E.A. acknowledges support as a Humboldt Research Fellowship for Experienced Researchers. S.C. thanks The Academy of Science of Turkey for financial support. Computations were performed at the National Center for High-Performance Computing of Turkey under Grant No. 5004132016.program.

---

[1] K. S. Novoselov, A. K. Geim, S. V. Morozov, D. Jiang, Y. Zhang, S. V. Dubonos, I. V. Grigorieva, and A. A. Firsov, Science **306**, 666 (2004).

[2] S. Cahangirov, M. Topsakal, E. Aktürk, H. Sahin, and S. Ciraci, Phys. Rev. Lett. **102**, 236804 (2009); H. Şahin, S. Cahangirov, M. Topsakal, E. Bekaroglu, E. Akturk, R. T. Senger, and S. Ciraci, Phys. Rev. B. **80**, 155453 (2009); M. Topsakal, E. Akturk, and S. Ciraci, *ibid.* **79**, 115442 (2009); E. Bekaroglu, M. Topsakal, S. Cahangirov, and S. Ciraci, *ibid.* **81**, 075433 (2010); M. Topsakal, S. Cahangirov, E. Bekaroglu, and S. Ciraci, *ibid.* **80**, 235119 (2009).

[3] Q. Fan, L. Yan, M. W. Tripp, O. Krejci, S. Dimosthenous, S. R. Kachel, M. Chen, A. S. Foster, U. Koert, P. Liljeroth, and J. M. Gottfried, Science **372**, 852 (2021).

[4] A. T. Balaban, C. C. Rentia, and E. Ciupitu, Rev. Roum. Chim. **13**, 231 (1968).

[5] M. A. Hudsepeth, B. W. Whitman, V. Barone, and J. E. Peralta, ACS Nano **4**, 4565 (2010).

[6] X-Q. Wang, H-D. Li, and J-T. Wang, Phys. Chem. Chem. Phys. **15**, 2024 (2013).

[7] O. Rahaman, B. Mortavazi, A. Dianat, G. Cuniberti, and T. Rabczuk, FlatChem **1**, 65 (2017).

[8] M. Shahrokhi, B. Mortazavi, and G. R. Berdiyorov, Solid State Commun. **253**, 51 (2017).

[9] G. Kresse and J. Furthmüller, Phys. Rev. B **54**, 11169 (1996).

[10] P. E. Blöchl, Phys. Rev. B **50**, 17953 (1994).

[11] J. P. Perdew, K. Burke, and M. Ernzerhof, Phys. Rev. Lett. **77**, 3865 (1996).

[12] H. J. Monkhorst and J. D. Pack, Phys. Rev. B **13**, 5188 (1976).

[13] A. V. Krukau, O. A. Vydrov, A. F. Izmaylov, and G. E. Scuseria, J. Chem. Phys. **125**, 224106 (2006).

[14] S. Grimme, J. Antony, S. Ehrlich, and S. Krieg, J. Chem. Phys. **132**, 154104 (2010).

[15] S. Grimme, S. Ehrlich, and L. Goerigk, J. Comput. Chem. **32**, 1456 (2011).

[16] D. Alfè, Comput. Phys. Commun. **180**, 2622 (2009).

[17] A. Togo and I. Tanaka, Scr. Mater. **108**, 1 (2015).

[18] V. Wang, N. Xu, J. C. Liu, G. Tang, and W.-T. Geng, Comput. Phys. Commun. **267**, 108033 (2021).

[19] U. Herath, P. Tavadze, X. He, E. Bousquet, S. Singh, F. Munoz, and A. H. Romero, Comput. Phys. Commun. **251**, 107080 (2020).

[20] R. C. Andrew, R. E. Mapasha, A. M. Ukpong, and N. Chetty, Phys. Rev. B **85**, 125428 (2012).

[21] C. Lee, X. Wei, J. W. Kysar, and J. Hone, Science **321**, 385 (2008).

[22] G. Gui, J. Li, and J. Zhong, Phys. Rev. B **78**, 075435 (2008).

[23] D. Liu, C. Daniels, V. Meunier, A. G. Every, and D. Tománek, Carbon **157**, 364 (2020).

[24] O. L. Blakslee, D. G. Proctor, E. J. Seldin, G. B. Spence, and T. Weng, J. Appl. Phys. **41**, 3373 (1970).

[25] C. Rêgo, L. Oliveira, P. Tereshchuk, and J. Da Silva, J. Phys.: Condens. Matter **27**, 415502 (2015).

[26] M. Hanfland, H. Beister, and K. Syassen, Phys. Rev. B **39**, 12598 (1989).

[27] R. Yan, Q. Zhang, W. Li, I. Calizo, and C. Richter, Appl. Phys. Lett. **101**, 022105 (2012).

[28] E. Mostaani, N. D. Drummond, and V. I. Fal'ko, Phys. Rev. Lett. **115**, 115501 (2015).

[29] S. Cahangirov, C. Ataca, M. Topsakal, H. Sahin, and S. Ciraci, Phys. Rev. Lett. **108**, 126103 (2012); S. Cahangirov, S. Ciraci, and V. O. Ozcelik, Phys. Rev. B **87**, 205428 (2013).

[30] Z. Liu, J. Z. Liu, Y. Cheng, Z. Li, L. Wang, and Q. Zheng, Phys. Rev. B **85**, 205418 (2012); L. Spanu, S. Sorella, and G. Galli, Phys. Rev. Lett. **103**, 196401 (2009); S. Lebegue, J. Harl, T. Gould, J. G. Angyan, G. Kresse, and J. F. Dobson, *ibid.* **105**, 196401 (2010).

[31] S. Cahangirov, V. O. Ozcelik, A. Rubio, and S. Ciraci, Phys. Rev. B **90**, 085426 (2014).

[32] T. Gorkan, E. Akturk, and S. Ciraci, Phys. Rev. B **100**, 125306 (2019).

[33] M. Aras, C. Kilic, and S. Ciraci, Phys. Rev. B **95**, 075434 (2017); J. Phys. Chem. C **122**, 1547 (2018).

[34] V. O. Özçelik and S. Ciraci, Phys. Rev. B **91**, 195445 (2015).